Biomaterials Science

PAPER

View Article Online
View Journal | View Issue

Cite this: *Biomater. Sci.*, 2019, **7**, 1179

Clickable PEG hydrogel microspheres as building blocks for 3D bioprinting†

Shangjing Xin,[a] David Chimene,[a] Jay E. Garza,[a] Akhilesh K. Gaharwar[a,b] and Daniel L. Alge *[a,b]

Received 12th October 2018,
Accepted 9th January 2019

DOI: 10.1039/c8bm01286e

rsc.li/biomaterials-science

Three-dimensional (3D) bioprinting is important in the development of complex tissue structures for tissue engineering and regenerative medicine. However, the materials used for bioprinting, referred to as bioinks, must have a balance between a high viscosity for rapid solidification after extrusion and low shear force for cytocompatibility, which is difficult to achieve. Here, a novel bioink consisting of poly(ethylene glycol) (PEG) microgels prepared *via* off-stoichiometry thiol–ene click chemistry is introduced. Importantly, the microgel bioink is easily extruded, exhibits excellent stability after printing due to interparticle adhesion forces, and can be photochemically annealed with a second thiol–ene click reaction to confer long-term stability to printed constructs. The modularity of the bioink is also an advantage, as the PEG microgels have highly tunable physicochemical properties. The low force required for extrusion and cytocompatibility of the thiol–ene annealing reaction also permit cell incorporation during printing with high viability, and cells are able to spread and proliferate in the interstitial spaces between the microgels after the constructs have been annealed. Overall, these results indicate that our microgel bioink is a promising and versatile platform that could be leveraged for bioprinting and regenerative manufacturing.

1. Introduction

Three-dimensional (3D) bioprinting has received great attention for manufacturing scaffolds with biofunctional components, such as therapeutic cells and growth factors, for tissue engineering.[1,2] This method allows printing of customized, patient-specific medical devices for the development of precision biomaterials and personalized medicine.[3] There are many reported 3D bioprinting strategies, including inkjet, stereolithography, and extrusion.[4–6] In general, the materials used in 3D bioprinting, which are referred to as bioinks, are polymer precursor solutions that can crosslink into a hydrogel network *via* UV polymerization, ionic exchange, or thermal gelation.[7–10] In extrusion bioprinting specifically, which is widely used due to its low cost and ease of adoption,[11] a good bioink needs to be extruded smoothly (printability), solidify rapidly to avoid collapse (stability), and have good biocompatibility.[12] Most extrusion-based bioinks are viscous solutions in order to maintain structural integrity after extrusion, but these materials can require high shear force during printing, which can negatively impact cell viability.[13–15]

Non-viscous precursor solutions, such as poly(ethylene glycol) (PEG) and hyaluronic acid (HA), are attractive base materials for bioinks because they can be encoded with cell-instructive cues for tissue engineering applications.[16–18] However, their lack of stability after extrusion is a challenge. One approach to improve the stability of non-viscous materials for extrusion bioprinting is nanoparticle reinforcement,[8,19] but these additives can potentially affect the cell response. Alternatively, photopolymerization at the needle tip during extrusion has been shown to improve the stability of PEG, HA, and gelatin bioinks without compromising cell viability.[20] Elegant strategies that leverage reversible crosslinking have also been reported. For example, Yin *et al.* used a low concentration of thermo-crosslinked methacrylated gelatin to maintain high cell viability and an additional irreversible UV crosslinking step to enhance the mechanical strength.[21] More recently, Lou *et al.* exploited the dynamic nature of hydrazone crosslinking and demonstrated that incorporating a biocompatible catalyst affords low viscosity during extrusion but results in stable constructs after the catalyst diffuses out of the material after printing.[22] Despite these efforts, the ability to print multi-layered structures (>10 mm tall) using non-viscous bioinks remains limited.

An alternative strategy that could circumvent the need to increase bioink viscosity is to use hydrogel microparticles (*i.e.*, microgels). Hinton *et al.* demonstrated that complex structures

---

[a] *Department of Biomedical Engineering, Texas A&M University, College Station, TX, 77843, USA. E-mail: dalge@tamu.edu*

[b] *Department of Materials Science and Engineering, Texas A&M University, College Station, TX, 77843, USA*

† Electronic supplementary information (ESI) available: Details of microgel formulations, experimental data of cell growth and adhesion on microgels, videos of microgel printing. See DOI: 10.1039/c8bm01286e

can be produced from non-viscous bioinks by printing into a bath of gelatin microgels, which provides a temporary support.[23] Strategies using microgels themselves as the bioink can also be envisioned. Several papers have reported that microgels can be injected into *in vivo* tissue cavities, indicating that they can be extruded with low shear forces, and further annealed into microporous hydrogels.[24–27] Highley *et al.* recently reported that densely packed microgels exhibit shear thinning properties and can be used as bioinks for 3D printing.[28] We recently reported the use of thiol–ene click chemistry for microgel annealing into 3D constructs.[29] Specifically, we showed that thiol–ene click chemistry could be leveraged to produce PEG microgels bearing unreacted norbornene groups, which could subsequently be annealed with a PEG-di-thiol linker *via* a second thiol–ene click reaction. We also demonstrated cell incorporation with high viability after annealing and showed that human mesenchymal stem cells (hMSCs) could spread, proliferate, and activate mechanosignaling pathways in response to the physicochemical properties of the PEG microgels. Based on these results, we believe that our clickable PEG microgels could be useful as a bioink for 3D printing.

The objective of this study was to evaluate the utility of clickable PEG microgels for 3D bioprinting. To this end, we used an electrospraying apparatus to produce batches of PEG hydrogel microspheres with varying size and physicochemical properties. We then optimized printing parameters for the microgel bioink to achieve consistent extrusion and printing of 3D structures. Because the PEG microgels contained unreacted norbornene groups, bis-thiol crosslinker and photoinitiator solutions were added onto the printed structure, and printed constructs were annealed to provide long-term stability. 3D anatomically sized shapes were printed to further demonstrate the utility of our microgel bioink. Finally, human mesenchymal stem cells (hMSCs) were incorporated in the microgel bioink during bioprinting to evaluate cytocompatibility of the process.

2. Experimental section

2.1 Materials

Four-arm PEG-norbornene (PEG-Nb) macromers were synthesized from PEG-hydroxyl precursors (JenKem Technology, 5, 10, and 20 kDa) by esterification with 5-norbornene-2-carboxylic acid (Alfa Aesar) and diisopropyl carbodiimide (Alfa Aesar), as previously described by Jivan *et al.*[30] The percent functionalization of PEG-Nb was greater than 95% determined by ^{1}H NMR spectroscopy analysis. PEG-dithiol (PEG-DT, 3400 Da) crosslinker was purchased from Laysan Bio. LAP was synthesized following the methods of Fairbanks *et al.* without modification and verified by ^{1}H NMR spectroscopy and electrospray ionization (ESI) mass spectrometry prior to use.[31] The cell adhesive peptide CGRGDS was prepared *via* microwave-assisted solid phase peptide synthesis and standard Fmoc methods. Peptide identity was verified using matrix-assisted laser desorption-ionization time-of-flight mass spectrometry (MALDI-TOF MS).

2.2 Microgel electrospraying

PEG microgel electrospraying setup was similar to the previously reported approach.[32] Based on the gel table (Table S1†), PEG-Nb and PEG-DT were mixed off-stoichiometrically so that 25% excess norbornene groups were available for further photocrosslinking of microgels. The mixed precursor solutions were electrosprayed into a bath of light mineral oil with Span 80 (0.5 wt%) and photopolymerized into microgels with UV irradiation (60 mW cm^{-2}, 365 nm). The UV light was kept on for 2 minutes after all precursor solutions were sprayed. The microgels were rinsed with phosphate buffered saline (PBS) three times and centrifuged at 4400 rpm for 5 minutes to remove the mineral oil. The microgels were stored in PBS at 4 °C and allowed to reach equilibrium swelling before use.

2.3. Microgel characterization

The morphology of the microgels was observed by confocal microscopy (FV1000, Olympus). For visualization, they were labeled with Alexa Fluor 488 NHS ester dye through amide linkage to CGRGDS peptide for 2 h at 4 °C. The size of microgels was measured from fluorescent images using Image-J software, and 50–100 microgels were examined for each group. Microgel pellets were also cryo-sectioned into 25 μm slices, and the Young's Modulus of the microgels was tested by AFM (Dimension Icon, Bruker) with a SiO2 colloidal probe (5 μm diameter, spring constants 0.6 N m^{-1}; Novascan).

2.4 3D printing of microgels

Printed shapes were designed in Solidworks and exported as STL files. STL files were loaded into Slic3r Prusa Edition 1.31.6 to customize printing options and converted into G-code printer instructions. Repetier-Host was used to interface with the 3D printer. The layer height was set to 500 μm, layer width was set at 600 μm, and the print speed was kept at 10 mm s^{-1}, or 0.27 mL min^{-1}. Pelleted microgel bioink was loaded into a 3 mL syringe and inserted into an extrusion tube. It was then extrusion printed through an I3 RepRap printer. Two nozzle tip sizes, 840 and 600 μm, were studied for microgel extrusion. Because the adhesive forces between the microgels could cause tearing as the print head moved, we manually added one drop of aqueous solutions onto printed structures every 10 layers. A 3 cm diameter honeycomb and a hollow 2 cm tall × outer diameter 10 mm and inner diameter 8 mm cylinder was printed from the microgel bioink. The microgel bioink was labeled with fluorescein NHS ester to visualize printed structures. An ear shape was printed with length of 4 cm, width of 2.7 cm, and height of 0.7 cm. A nose shape was printed with length of 3.5 cm, width of 2.3 cm, and height of 1.4 cm. The infill density of ear and nose printing is 60%.

2.5 Thiol–ene click annealing of printed structures

PEG-DT and LAP solutions were pipetted onto printed structures, which were then photopolymerized under UV irradiation

(60 mW cm^{-2}, 365 nm, 3 min) to link the microgels together. The storage modulus of printed microgel disks was measured before and after photopolymerization on a rheometer (Physica MCR 301, Anton Paar) under a time sweep at 1% strain and 1 rad s^{-1}. The weight and diameter of microgel disks were also measured at different time points to compare the swelling properties with bulk hydrogels.

2.6 hMSC culture and printing

hMSCs (P1) were purchased from the Institute for Regenerative Medicine at Texas A&M University and expanded in low-glucose Dulbecco's modified Eagle's medium (DMEM) with 10% fetal bovine serum (FBS), 50 U ml^{-1} penicillin, 50 μg ml^{-1} streptomycin and 1 ng ml^{-1} fibroblast growth factor (bFGF, Sigma) at 37 °C and 5% CO_2 in a humidified environment. hMSCs were used up to passage 5. In the experiments characterizing the effects of microgel properties on cell–material interactions, hMSCs (5×10^5 cells per well) were cultured with microgels in 24-well ultra-low binding plates (Costar) and allowed good mixture with gentle shaking at 20 rpm for first 2 h. Cell-culture plates were then removed from shaker and cultured for another 22 h. Samples were fixed using 4% formaldehyde for 15 min at room temperature. Focal adhesion was assessed by immunohistochemistry utilizing antibodies against anti-vinculin (1 : 1000, EMD Millipore). Goat anti-mouse fluorescein (1 : 100, Jackson ImmunoResearch) was used as fluorescent secondary antibody to visualize the location of the primary antibody. Cytoskeletal staining was performed using rhodamine phalloidin (1 : 40, Invitrogen) with counter staining of 4′,6-diamidino-2-phenylindole (DAPI) (1 : 1000, Biolegend). Quantification of focal adhesion formation was performed on images captured at 20× magnification using Image-J software. Representative images are shown in Fig. S2.† The Threshold and Analyze Particles functions were used to determine total area of focal adhesion per cell in maximum intensity *Z*-projection images. At least 50 cells were measured per group. Student's *t*-test was used to determine significant differences between two groups. Significance is indicated by * corresponding to $p < 0.01$.

For the printing experiment, an hMSC suspension (5×10^6 cells per mL) was mixed with microgels for 30 min before adding into extrusion tube. The extrusion printing method was similar as described above and a 4-layer honeycomb shape was printed. hMSC viability in the printed structure was assessed at 1 hour, 1, 5, and 10 days using Live/dead kit (L3224, Invitrogen) and confocal microscope (FV1000, Olympus). Quantification of viability was performed using Image-J software, and at least 200 cells were calculated for each group.

3. Results and discussion

3.1 Production of microgel bioinks by electrospraying

In order for microgel printing to be feasible, the microgel fabrication method should be amenable to producing large batches of microgels with tunable properties. To address this challenge, we utilized electrospraying to prepare PEG microgels, as we were able to employ large flow rates up to 12 mL h^{-1}, which was more suitable for producing large-scale batches needed for bioprinting compared to other microgel synthesis methods, such as microfluidics.[24,32,33] In addition, we chose thiol–ene click chemistry to crosslink the PEG microgels, as this strategy enables us to easily tune the physicochemical properties of the microgels, control the stoichiometry, and also offers fast reaction kinetics.[31,34] This allows for immediate gelation after electrospraying to stabilize the droplets, unlike other click reactions, such as thiol-Micheal addition and strain-promoted azide–alkyne crosslinking. During electrospraying, off-stoichiometric non-viscous PEG precursor solutions were sprayed into small droplets from a blunted needle submerged in mineral oil and photocrosslinked immediately upon UV irradiation (Fig. 1a). This approach resulted in norbornene bearing PEG microgels, which is important because it enables us to use a second thiol–ene reaction to anneal and strengthen a 3D printed microgel structure.

The average sizes of electrosprayed microgels from varying electrospraying parameters and properties of precursor solutions were characterized by microscopy and image analysis software (Fig. 2). Voltage, flow rate, tip-to-grounded ring distance, and needle gauge were studied, as well as molecular weight of PEG-Nb (resulting in various viscosity). 5, 10, and 20 kDa PEG-Nb were used to prepare microgels and termed PEG5, PEG10, and PEG20, respectively. As we tune the stiffness of microgels by adjusting molecular weight of PEG-Nb, it is important to have comprehensive size characterization data so that we can choose appropriate parameters for manufacturing desirable sized microgels with varying stiffness. Fig. 2a demonstrates an overall decreasing size trend with increasing voltage. The applied electric field could affect the shape of the induced Taylor cone and liquid jetting. Low voltage did not help to form a sharp Taylor cone and the resulting microgels were much larger. In addition, Fig. 2b and c presents an increasing size trend with increasing flow rate while decreasing needle gauge. Both conditions would also influence the formation of the Taylor cone and, thus, the size of resulting microgels. However, the tip-to-grounded ring distance did not affect the average size of microgels (Fig. 2d), which indicated that the submerged oil environment provided a stable and consistent electric field independent of distance. Fig. 2e shows that the average size of microgels increased when using larger molecular weight PEG-norbornene (PEG-Nb). As indicated in the gel table (Table S1†), PEG20 precursor solutions contained less crosslinker and, thus, had a lower viscosity compared to PEG5 and PEG10. Therefore, formation of the Taylor cone was hindered under the same voltage conditions, because of the high fluidity resulting in larger average microgel sizes. Fluorescence microscopy imaging of Alexa Fluor 488-labeled microgels further verified the difference in size distribution resulting from varying conditions. It is notable that all groups show a wide size distribution with roughly 30% standard deviation. However, this does not impair their utility in 3D printing as

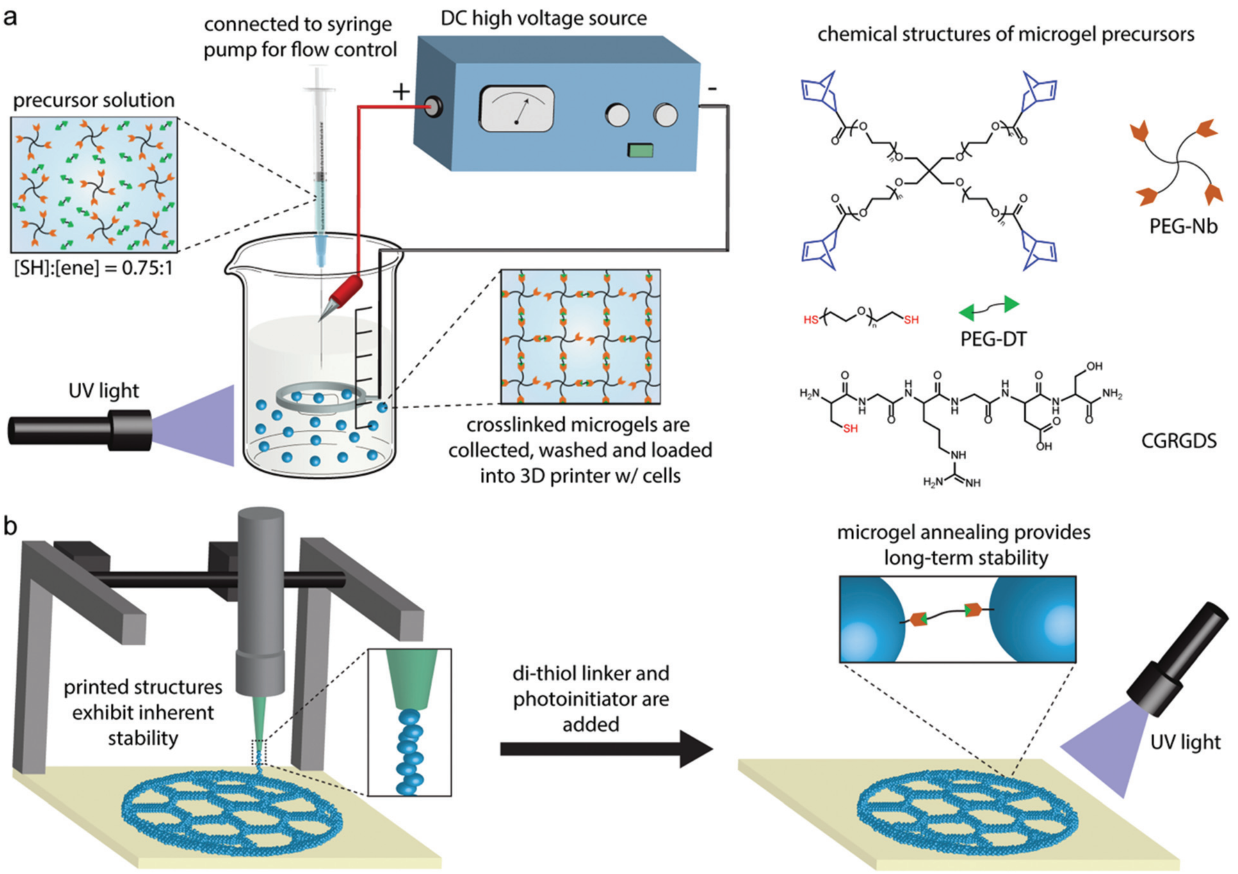

Fig. 1 Overview of clickable PEG microgel bioink production and use in 3D printing. (a) Chemical structures and schematic of the submerged electrospraying setup for synthesizing PEG microgels *via* thiol–ene click chemistry. (b) Schematic of PEG microgel 3D printing procedure. Printed structures exhibit inherent stability due to the cohesive forces between PEG microgels. Long-term stability is achieved by annealing the microgels with a second thiol–ene reaction that crosslinks the microgels.

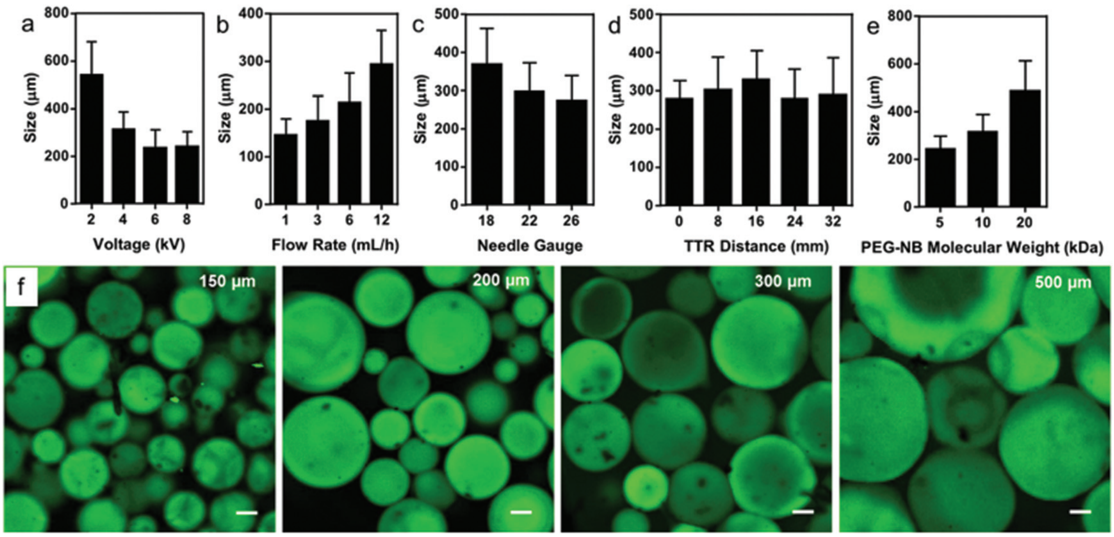

Fig. 2 Electrosprayed PEG microgel bioink size is controlled by varying electrospraying parameters and PEG molecular weight. Size distributions of microgels fabricated by varying (a) voltage, (b) flow rate, (c) needle gauge, (d) tip-to-ring distance, and (e) molecular weight of PEG-Nb. The fixed parameters were 5 kDa PEG-Nb, 4 kV voltage, 12 mL h^{-1} flow rate, 22 needle gauge, and 16 mm TTR distance. (f) Representative fluorescence images of microgels with different sizes (approximate average size is noted). Microgels were labeled by Alexa Fluor 488-succinimidyl ester dye. Scale bars are 50 µm.

the main purpose of using these microgels is to provide structural integrity of printed constructs.

Before proceeding to printing experiments, we cultured hMSCs on PEG microgels with varying biophysical and biochemical properties to evaluate the effects of bioink properties on cell–material interactions (Fig. 3). hMSCs were allowed to interact with microgels in a low-binding plate. Microgels were prepared with and without RGD cell-adhesive peptide and with varying stiffness by adjusting the molecular weight of PEG-Nb. The results showed hMSCs could attach and spread on RGD-presenting microgels, whereas they tended to aggregate into cell clusters and did not interact with microgels lacking RGD (Fig. 3a and S1†). Furthermore, the Young's modulus of microgels were characterized by nanoindentation with atomic force microscopy (Fig. 3b). Spreading of hMSCs also varied when seeded onto microgels with varying stiffness. They tended to spread more and exhibit higher density of focal adhesions on the surface of stiffer microgels compared to softer microgels (Fig. 3c and d). Collectively, these results indicated that the physicochemical properties of the microgels can be tuned to modulate cell behavior, which could be potentially leveraged during 3D bioprinting.

3.2 Printability of microgel bioinks

To evaluate microgel printability, we loaded a batch of electrosprayed microgels into a 3 mL syringe, which was then installed onto an extrusion-based 3D printer, as shown in Fig. 1b. The motor-driven 3D printer used here is a low-cost setup that can precisely extrude microgels based on volume. The printability of the microgel bioink was studied and optimized from 1D filament extrusion, followed by 2D honeycomb printing, and lastly 3D cylinder printing (Fig. 4). Since the microgel size would alter the required printing parameters, such as nozzle size and extrusion rate, we utilized only 200 μm sized PEG5 microgels from the set of electrospraying parameters characterized above to demonstrate the general approach of microgel printing.

First, a microgel extrusion study was performed to form a vertical line hanging from two different sized nozzles (Fig. 4a, Video S1 and 2†). The inner diameters of the large and small nozzles were 840 and 600 μm, respectively. The microgels formed a continuous line and extruded consistently from the large nozzle. The extruded filament from the large nozzle was also consistently 3 cm long before dropping due to gravity. In contrast, when the smaller nozzle was used, the extrusion was uneven and some microgels became stuck during extrusion. Thus, we concluded that the nozzle size needs to be at least 4-fold larger than the average size of the microgels to achieve consistent extrusion.

Second, 2D honeycomb-shape printing was performed to test whether the extrusion would be continuous when the nozzle was moving during printing (Fig. 4b). An intact three-layer honeycomb structure was successfully printed when microgels were extruded. A quantification of width variability on the entire honeycomb construct was performed by analyzing 50 different locations, and the average width was 779 μm with a standard deviation of 140.7 μm, most likely due to the large size of the microgels. In addition, a magnified view of an

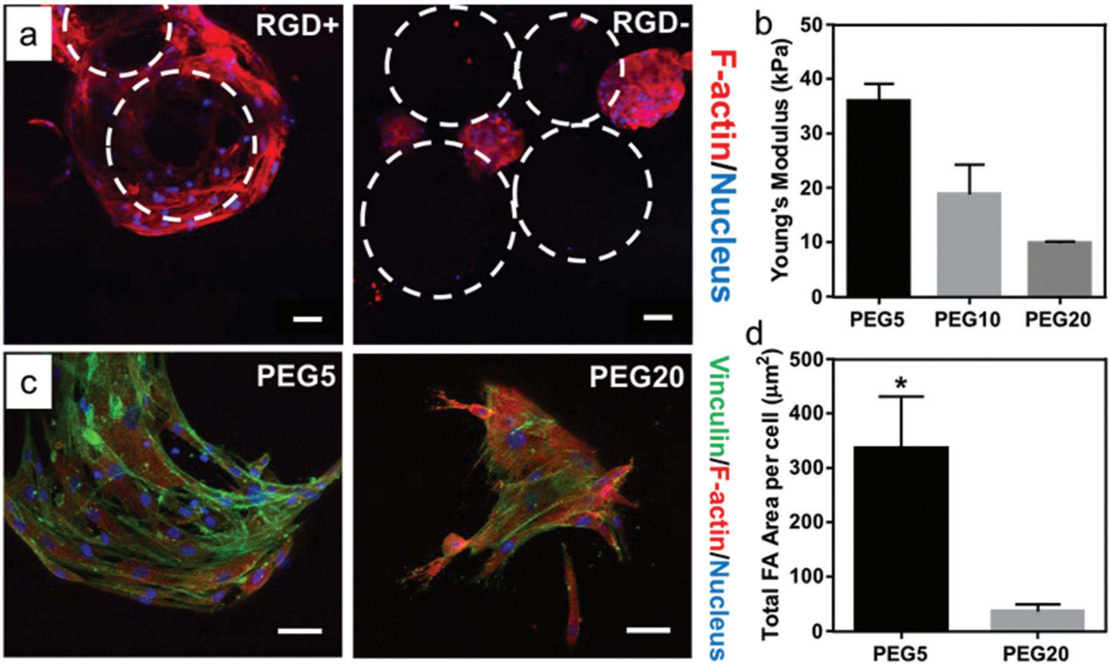

Fig. 3 hMSCs show varied responses on microgels with tunable properties. (a) Fluorescence microscopy images showing hMSC adhesion on microgels with and without the RGD peptide. (b) Mechanical properties of microgels prepared with varying molecular weight of PEG-Nb and measured by AFM. (c) hMSC spreading morphology and (d) focal adhesion quantification on microgels with varying modulus. Scale bars are 50 μm. Significance is indicated by * corresponding to $p < 0.01$.

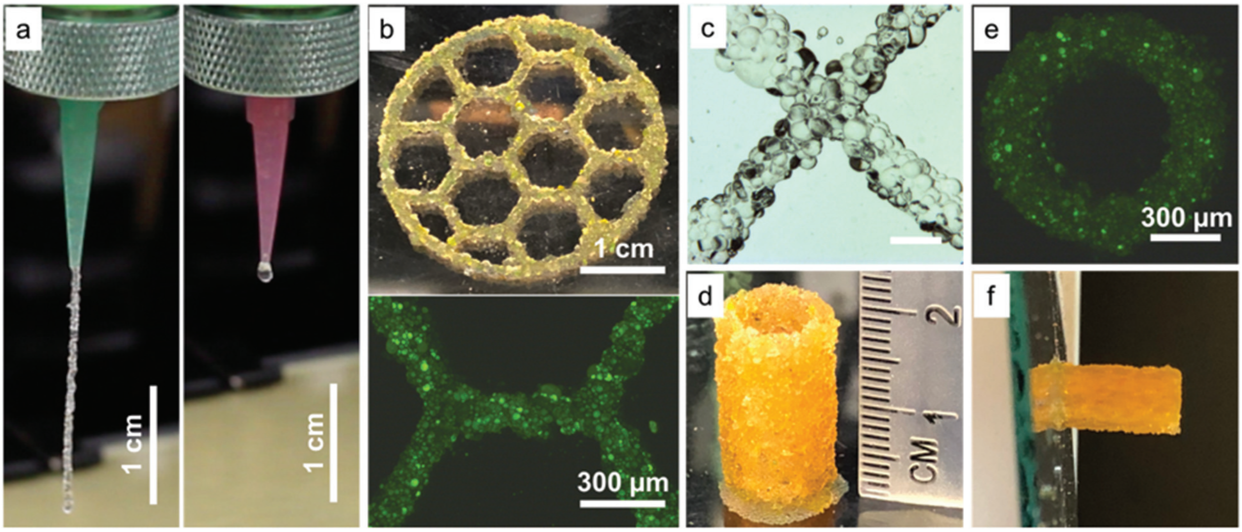

Fig. 4 Optimized printing parameters achieve consistent microgel bioink extrusion and cohesive constructs with mechanical stability. (a) A vertical filament of microgel bioink extruded using varying nozzle sizes. The inner diameters of the green and pink nozzles were 840 and 600 µm, respectively. Video S1 and 2† further illustrates the comparison of extrusion consistency. (b) Three-layer honeycomb printing with a fluorescent zoom-in image. (c) Stereomicroscopy image showing an intersection point of two microgel filaments. Scale bar is 600 µm. (d) Cylindrical shape printing with 1 cm outer diameter and 0.8 inner diameter illustrating microgel printing can achieve 20 mm in height. (e) Fluorescent image showing top view of the printed cylinder. (f) Printed cylinder on a tilted glass (85°) without falling demonstrating outstanding stability of microgel printing.

intersection point between two lines is provided to demonstrate that microgel printing produces filaments with clean overlap on each other (Fig. 4c).

Next, we tested the *Z*-axis structural integrity and stability of microgel structures by printing a 1 cm diameter cylindrical shape (Fig. 3d, a high aspect ratio structure). The images showed that microgel printing was able to achieve a cylindrical shape with a clean ring structure from the top view (Fig. 3d and e). Remarkably, the microgel printed structure exhibited excellent stability and could support a height of 2 cm (40 layers) without collapsing, which was at least twice as high as previously reported literature on printing of non-viscous materials without using supporting gels.[20,35] Moreover, the printed cylinder did not fall when we titled the glass surface it was printed on by 90° (Fig. 3f and Video S3†), demonstrating outstanding stability and strong adhesion between microgels. This result is particularly interesting in light of the recent work of Highley *et al.* demonstrating high printing fidelity of smaller, monodispersed microgel inks,[28] as we believe that the polydispersity of our microgels may facilitate jamming and cohesion after extrusion. This variable will be examined in the future to understand potential trade-offs between microgel polydispersity and print resolution for various applications.

While multi-layer structures could be fabricated due to the natural cohesiveness of the microgels, the clickable nature of the microgels enables annealing to confer long-term stability to the construct. To this end, we added a mixture of PEG-dithiol linker and photoinitiator to the constructs during printing and then applied UV irradiation to anneal the microgels *via* their unreacted norbornene groups (see section 2.5). Storage modulus measurements *via* rheology on printed disk-shaped microgel structures showed a 1.6-fold increase in modulus after UV annealing (Fig. 5a), which verified that the printed microgel structure was strengthened and connected as an intact construct. Importantly, the crosslinked constructs also exhibited excellent geometric stability after annealing due to their non-swelling nature, since the microgels were allowed to swell to equilibrium before printing (Fig. 5b and c). This feature could be important for the development of geometrically constrained structures, such as tubular channels.[36] Future work will investigate this possibility, as well as the possibility of using smaller sized and more monodispersed microgels to print constructs with refined structures.

3.3 3D printing complex and cell-laden structures

We also explored using our microgel bioink to print geometrically complex and anatomically relevant 3D structures. Fig. 6a shows an anatomically sized 3D printed ear from our microgel bioink, which exhibited high fidelity and stability even without secondary crosslinking. The helix of the printed ear demonstrates the overhang structure in the ear, further illustrating the outstanding stability from the cohesive forces between microgels. Fig. 6b presents an anatomically sized 3D printed nose from our microgel bioink. The clean curve on the surface of the nose and the precise shape of nostril further verify the high printability of our microgel bioink and its utility for producing anatomically relevant tissue structures. A comparison of overall dimensions and special features for both ear and nose printing is provided in Fig. 6c. Both printed structures were roughly 5% larger in any dimension than the designed shape. The reason for this 5% error is possibly due to the slightly high infill density, which was used to ensure a consist-

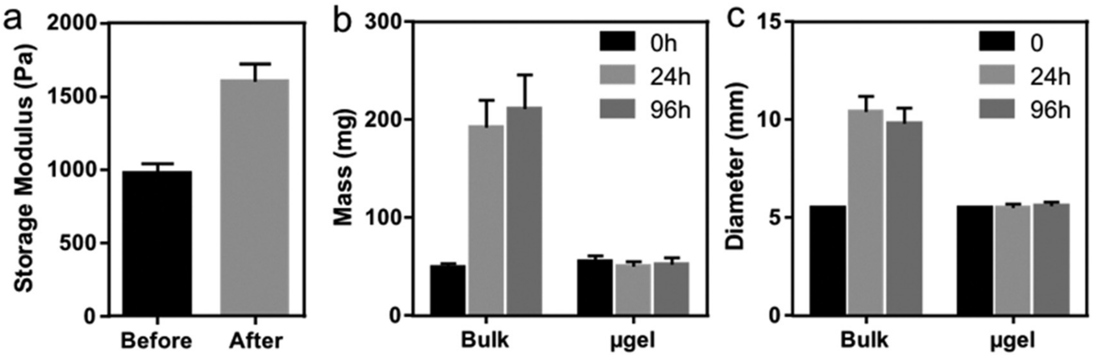

Fig. 5 Crosslinked constructs from microgel bioinks exhibit enhanced mechanical properties and non-swelling properties. (a) Storage modulus of printed microgel disks before and after photopolymerization. The swelling properties were compared between bulk hydrogel and microgel printed disks as measured in (b) mass and (c) diameter.

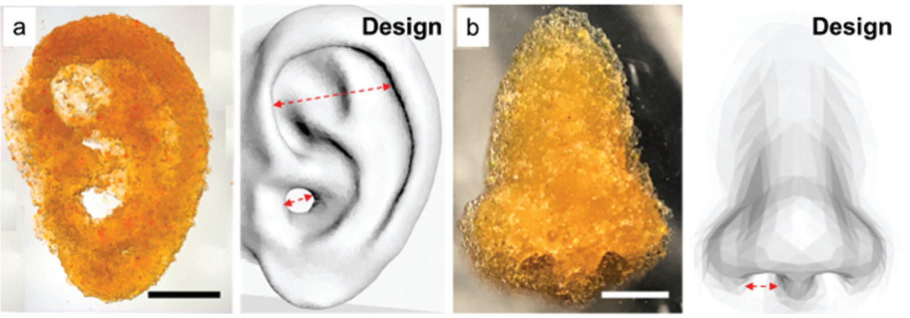

c

	Ear			Nose	
	Dimension (cm, L × W × H)	Helix (cm)	Canal (cm)	Dimension (cm, L × W × H)	Nostril (cm)
Designed Value	4 × 2.7 × 0.7	1.31	0.41	3.5 × 2.3 × 1.4	0.42
Actual Value	4.15 × 2.85 × 0.719	1.35	0.46	3.5 × 2.49 × 1.48	0.42

Fig. 6 Complex and anatomically relevant 3D structures can be produced with the PEG microgel bioink. (a) A 3D printed ear shape from microgel bioink showing mechanical stability and high fidelity. (b) A 3D printed nose shape from microgel bioink showing mechanical stability. The microgels were labeled with fluorescein and appear orange color. The scale bars are 1 cm. (c) Table comparing the designed and measured dimensions for both ear and nose printing. The ear helix and canal and nostril measurements were made as indicated with the double arrow lines.

ent flow of microgel bioink during printing. Although we did not explore it here, additional complexity could be easily achieved by leveraging the modularity of the microgels. Distinct formulations of microgels with different stiffness or presenting different chemical ligands could be combined in a multi-layered construct either randomly or with spatial control to recapitulate native tissue structures and direct cellular behavior within the materials.

Finally, to test cytocompatibility, we incorporated hMSCs with our microgel bioink to print a multi-layered honeycomb structure. For this experiment, hMSCs were incubated with PEG5 microgels for 30 minutes, after which they were transferred to the extrusion syringe for printing. A four-layer honeycomb shape was then printed with 2 mm height so that hMSCs were incorporated within the 3D structure, and it was annealed before adding media. The viability of hMSCs in the printed honeycomb shape were evaluated by Live/Dead staining and fluorescence microscopy (Fig. 7). Fig. 7a shows a representative image of hMSCs growing in a corner of one hexagon after 5 days, and the cells exhibit excellent spreading and viability. Quantitative analysis of the Live/Dead staining indicated that the hMSC viability exceeded 88% at 1 hour, 80% at 1 day and 90% at 5 and 10 days (Fig. 7b), which is identical with our previous data on cell incorporation in microgel-based scaffolds,[29] indicating that cell viability was not compromised by harmful shear forces during microgel extrusion. In addition, although our microgel bioink was not degradable, the hMSCs continued to proliferate during culture in non-degradable microgel printed structures due to the microporosity (Fig. 7c). These results verified that our microgel bioink exhibits good cytocompatibility and is suitable for 3D bioprinting. Future studies will investigate the use of microgels syn-

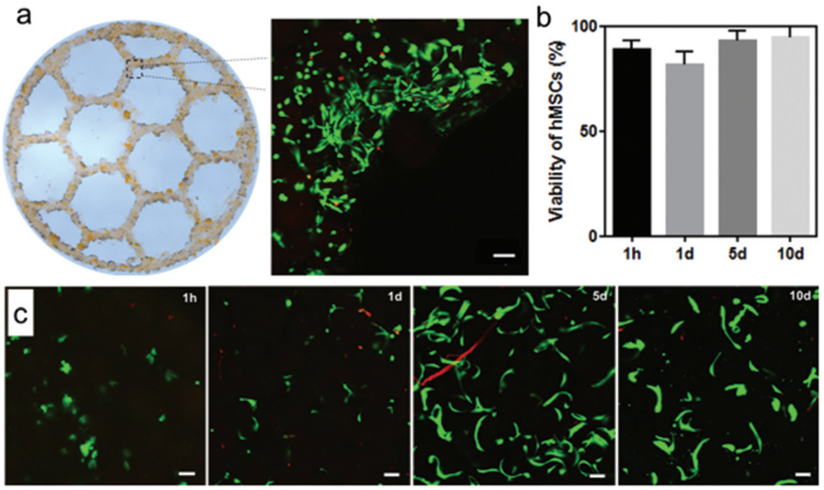

Fig. 7 Microgel bioink printing and annealing are cytocompatible. (a) *Z*-Projection image of Live/dead stained hMSCs growing at a corner of hexagon in a bioprinted honeycomb shape 5 days after printing. The *Z*-stack depth is 500 μm (scale bar = 100 μm). (b) Quantitative data of hMSC viability after microgel bioprinting. (c) *Z*-Projection images of live/dead stained hMSCs cultured in microgel printed disks at 1 hour, 1, 5, and 10 days. The *Z*-stack depths are 200 μm (scale bars = 50 μm).

thesized with degradable crosslinkers, such as matrix metalloproteinase-degradable peptides to permit cell-mediated degradation.

4. Conclusions

We report here a novel PEG microgel-based bioink for 3D printing. The microgels, which are produced by electrospraying and off-stoichiometric thiol–ene click chemistry, can be easily extruded and quickly stabilize after extrusion due to inherent cohesive forces between the microgels, thereby permitting the formation of complex and anatomically relevant 3D structures. Moreover, owing to the presence of unreacted norbornene groups, they can be annealed *via* a second thiol–ene click reaction to impart long-term stability, and the entire process is cytocompatible. Based on these results, clickable microgel bioinks could be a promising platform for large-scale artificial tissue or scaffold fabrication. Toward this goal, future studies should determine optimal printing parameters for other clickable PEG microgel formulations beyond what was studied here. The ability to guide cell patterning within microgel printed structures for specific applications and tissue types should also be explored.

Conflicts of interest

There are no conflicts to declare.

Acknowledgements

This research was supported by the National Institutes of Health (R21 AR071625 to D. L. A., DP2 EB026265 and R03 EB02345 to A. K. G.), the National Science Foundation (CMMI 1634858 to D. L. A. and CBET 1705852 to A. K. G.) and Texas A&M Engineering Experiment Station (start-up funds to D. L. A.). D. C. would like to acknowledge funding from the Texas A&M System Louis Stokes Alliance for Minority Participation (TAMUS LSAMP). We would like to thank Dr Wilson Serem at Materials Characterization Facility of TAMU for assistance with AFM testing and Dr Louise Abbott at College of Veterinary Medicine of TAMU for cryo-sectioning of the microgel pellets. We also thank Hector Perez at BME of TAMU for assistance with microgel fabrication.

References

1 Y. S. Zhang, K. Yue, J. Aleman, K. Mollazadeh-Moghaddam, S. M. Bakht, J. Yang, W. Jia, V. Dell'Erba, P. Assawes and S. R. Shin, *Ann. Biomed. Eng.*, 2017, **45**, 148–163.
2 N. J. Castro and D. W. Hutmacher, *Adv. Funct. Mater.*, 2018, **28**, 1703905.
3 B. A. Aguado, J. C. Grim, A. M. Rosales, J. J. Watson-Capps and K. S. Anseth, *Sci. Transl. Med.*, 2018, **10**, eaam8645.
4 A. K. Miri, D. Nieto, L. Iglesias, H. Goodarzi Hosseinabadi, S. Maharjan, G. U. Ruiz-Esparza, P. Khoshakhlagh, A. Manbachi, M. R. Dokmeci and S. Chen, *Adv. Mater.*, 2018, **30**, 1800242.
5 S. F. S. Shirazi, S. Gharehkhani, M. Mehrali, H. Yarmand, H. S. C. Metselaar, N. A. Kadri and N. A. A. Osman, *Sci. Technol. Adv. Mater.*, 2015, **16**, 033502.
6 S. V. Murphy and A. Atala, *Nat. Biotechnol.*, 2014, **32**, 773.
7 S. Bertlein, G. Brown, K. S. Lim, T. Jungst, T. Boeck, T. Blunk, J. Tessmar, G. J. Hooper, T. B. Woodfield and J. Groll, *Adv. Mater.*, 2017, **29**, 1703404.

8 D. Chimene, C. W. Peak, J. L. Gentry, J. K. Carrow, L. M. Cross, E. Mondragon, G. B. Cardoso, R. Kaunas and A. K. Gaharwar, *ACS Appl. Mater. Interfaces*, 2018, **10**, 9957–9968.

9 J. Jang, J. Y. Park, G. Gao and D.-W. Cho, *Biomaterials*, 2018, **156**, 88–106.

10 P. S. Gungor-Ozkerim, I. Inci, Y. S. Zhang, A. Khademhosseini and M. R. Dokmeci, *Biomater. Sci.*, 2018, **6**, 915–946.

11 J. K. Placone and A. J. Engler, *Adv. Healthcare Mater.*, 2018, **7**, 1701161.

12 X. Zhai, C. Ruan, Y. Ma, D. Cheng, M. Wu, W. Liu, X. Zhao, H. Pan and W. W. Lu, *Adv. Sci.*, 2018, **5**, 1700550.

13 S. A. Wilson, L. M. Cross, C. W. Peak and A. K. Gaharwar, *ACS Appl. Mater. Interfaces*, 2017, **9**, 43449–43458.

14 L. L. Wang, C. B. Highley, Y. C. Yeh, J. H. Galarraga, S. Uman and J. A. Burdick, *J. Biomed. Mater. Res., Part A*, 2018, **106**, 865–875.

15 N. R. Gandavarapu, D. L. Alge and K. S. Anseth, *Biomater. Sci.*, 2014, **2**, 352–361.

16 C. M. Madl and S. C. Heilshorn, *Adv. Funct. Mater.*, 2018, **28**, 1706046.

17 C. M. Madl, S. C. Heilshorn and H. M. Blau, *Nature*, 2018, **557**, 335–342.

18 T. E. Brown and K. S. Anseth, *Chem. Soc. Rev.*, 2017, **46**, 6532–6552.

19 X. Kuang, K. Chen, C. K. Dunn, J. Wu, V. C. Li and H. J. Qi, *ACS Appl. Mater. Interfaces*, 2018, **10**, 7381–7388.

20 L. Ouyang, C. B. Highley, W. Sun and J. A. Burdick, *Adv. Mater.*, 2017, **29**, 1604938.

21 J. Yin, M. Yan, Y. Wang, J. Fu and H. Suo, *ACS Appl. Mater. Interfaces*, 2018, **10**, 6849–6857.

22 J. Lou, F. Liu, C. D. Lindsay, O. Chaudhuri, S. C. Heilshorn and Y. Xia, *Adv. Mater.*, 2018, **30**, 1705215.

23 T. J. Hinton, Q. Jallerat, R. N. Palchesko, J. H. Park, M. S. Grodzicki, H.-J. Shue, M. H. Ramadan, A. R. Hudson and A. W. Feinberg, *Sci. Adv.*, 2015, **1**, e1500758.

24 D. R. Griffin, W. M. Weaver, P. O. Scumpia, D. Di Carlo and T. Segura, *Nat. Mater.*, 2015, **14**, 737.

25 L. R. Nih, E. Sideris, S. T. Carmichael and T. Segura, *Adv. Mater.*, 2017, **29**, 1606471.

26 J. E. Mealy, J. J. Chung, H. H. Jeong, D. Issadore, D. Lee, P. Atluri and J. A. Burdick, *Adv. Mater.*, 2018, **30**, 1705912.

27 L. Riley, L. Schirmer and T. Segura, *Curr. Opin. Biotechnol.*, 2019, **60**, 1–8.

28 C. B. Highley, K. H. Song, A. C. Daly and J. A. Burdick, *Adv. Sci.*, 2018, 1801076.

29 S. Xin, O. M. Wyman and D. L. Alge, *Adv. Healthcare Mater.*, 2018, **7**, 1800160.

30 F. Jivan, R. Yegappan, H. Pearce, J. K. Carrow, M. McShane, A. K. Gaharwar and D. L. Alge, *Biomacromolecules*, 2016, **17**, 3516–3523.

31 B. D. Fairbanks, M. P. Schwartz, C. N. Bowman and K. S. Anseth, *Biomaterials*, 2009, **30**, 6702–6707.

32 A. S. Qayyum, E. Jain, G. Kolar, Y. Kim, S. A. Sell and S. P. Zustiak, *Biofabrication*, 2017, **9**, 025019.

33 C. J. Young, L. A. Poole-Warren and P. J. Martens, *Biotechnol. Bioeng.*, 2012, **109**, 1561–1570.

34 L. A. Sawicki and A. M. Kloxin, *Biomater. Sci.*, 2014, **2**, 1612–1626.

35 W. Liu, Z. Zhong, N. Hu, Y. Zhou, L. Maggio, A. K. Miri, A. Fragasso, X. Jin, A. Khademhosseini and Y. S. Zhang, *Biofabrication*, 2018, **10**, 024102.

36 B. Trappmann, B. M. Baker, W. J. Polacheck, C. K. Choi, J. A. Burdick and C. S. Chen, *Nat. Commun.*, 2017, **8**, 371.